Marine and Petroleum Geology 145 (2022) 105849

Contents lists available at ScienceDirect

Marine and Petroleum Geology

journal homepage: www.elsevier.com/locate/marpetgeo

Discrete element method simulation of the fold-and-thrust belts along strike various compression in the southern margin of the Junggar Basin, China

Zhuoyi Shen [b], Fusheng Yu [a,b,*], Qianjun Wang [c], Jingqi Zhang [b], Yan Xue [c]

[a] State Key Laboratory of Petroleum Resources and Prospecting, China University of Petroleum (Beijing), Beijing, China
[b] Department of Earth Sciences, China University of Petroleum (Beijing), Beijing, China
[c] Exploration and Development Research Institute of Shengli Oilfield Company, SINOPEC, Dongying City, Shandong Province, China

ARTICLE INFO

Keywords:
3D numerical simulation
Discrete element method
Fold-and-thrust belt
Transfer zone
Junggar basin

ABSTRACT

The fold-and-thrust belts developed in the southern margin of the Junggar Basin in China can be divided into different segments and oblique rows in the strike and dip direction respectively. The internal structural patterns and linkage types of different sub-segments usually affect the oil and gas accumulation. In this work, we study on the propagation and linkages of the structural patterns involved in the fold-and-thrust belts due to the differential compression by the Discrete element method (DEM). Two simulations are configured to use four velocity modules, which can move with different velocity at the same time: (i) the homogenous module filled with brittle simulating sediment is used to investigate the structural response to a velocity difference and (ii) the module with ductile detachment at the front of each module is used to test how the weak layer affects deformation. The results are illustrated by topography of the simulations, such as cross sections perpendicular and parallel to the shortening direction, forward and lateral displacements seen from the top view, and sections of the velocity field. The results show that (i) resistance from adjacent modules promotes the development of back-thrusts in faster modules, and drag from faster moving module hinders nucleation in slower modules, and (ii) two types of transfer zones caused by shear stress appear in the piedmont region and in front of the fold belts. The detachment simulation produces results are similar to the western segment of the southern margin of the Junggar Basin, which can explain the several rows of anticlines that appear oblique in the plane. These results are useful to analyze the formation process of the oil and gas trap developed in the similar compressional area.

1. Introduction

Collisional mountains have been important for hydrocarbon geological research as a result of providing some information of the reservoir evolution (Bose and Mukherjee, 2020; Razavi Pash et al., 2021; Reber et al., 2021), and detail structural understanding of such area is quite useful for oil and gas exploration. Strike-slip fault zones may occur in these orogen systems, especially transfer faults, which cut off thrusts (Benesh et al., 2014) and cause a variable amount of shortening perpendicular to the wedge. Adjacent to different sediments, the distribution range or properties of the viscous materials, the geometry of backstops, the surface topography, and the pre-existing impediments can cause varying amounts of shortening in the lateral direction at the front of the intenders, which produces transfer faults (Calassou et al., 1993; Zweigel., 1998; Reiter et al., 2011; Sun et al., 2016; Borderie et al., 2018). Several typical transfer faults cutting off the fold and thrust belts developed from the northern margin of the Tianshan to the southern margin of the Junggar Basin can be determined from the regional geological map and satellite photos (Fig. 1A).

As shown by outcrops, borehole data and seismic interpretation, the stratigraphic succession in this area consists of, in ascending order, the Carboniferous, Permian, Triassic, Jurassic, Cretaceous, Paleogene, Neogene and quaternary which is characterized by thickening to the foredeep and development of syn-depositional deformation (Yu et al., 2009) (Figs. 1C and 2). The mudstone and coal layers developed in the Badaowan, Sangonghe and Xishanyao formations in the bottom of the Jurassic system to act as detachment layers (Figs. 2 and 1C).

According to the differences of structural deformation, the northern margin of the Tianshan can be divided into two segments by the transfer fault (TF_1) from east to west (Fig. 1B). Arcuate thrust-and-fold belts that protrude to the north are developed in the eastern segment. Three oblique rows of thrust-and-fold belts are in the western segment which is

* Corresponding author. State Key Laboratory of Petroleum Resources and Prospecting, China University of Petroleum (Beijing), Beijing, China.
E-mail address: fushengyu@cup.edu.cn (F. Yu).

https://doi.org/10.1016/j.marpetgeo.2022.105849
Received 4 March 2022; Received in revised form 22 July 2022; Accepted 22 July 2022
Available online 21 August 2022

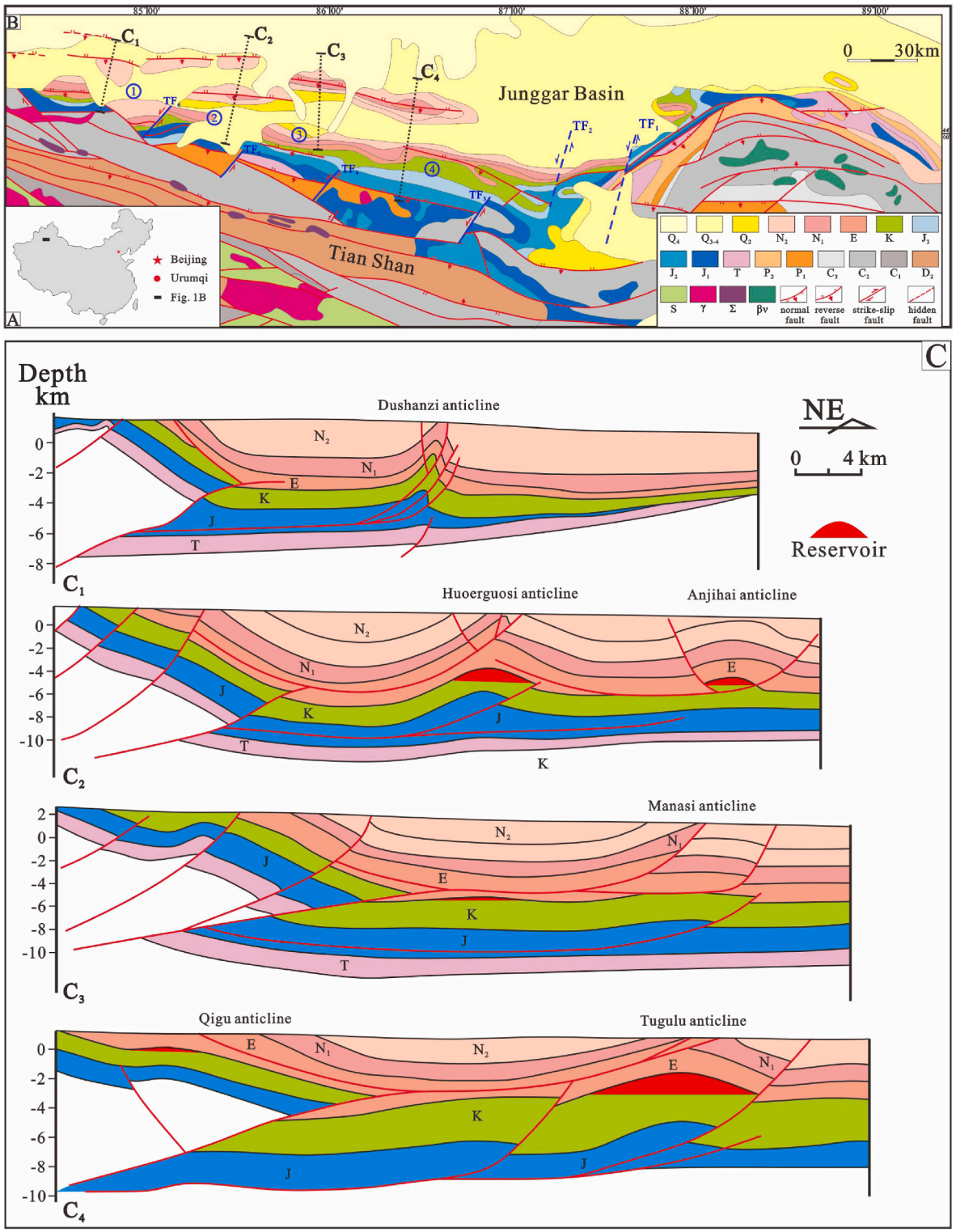

Fig. 1. A) Simplified location map of the southern margin of the Junggar Basin, China. B) Geological map of fold-and-thrust belts in the southern margin of Junggar Basin (see location in Fig.1A). C) Interpreted structural cross sections cutting through the western segment in the southern margin of the Junggar Basin (see location in Fig.1B) (modified from Yu et al., 2012).

divided into several sub-segments by transfer faults ($TF_{2\text{-}6}$). The first row consisting of the Qigu and Tuositai anticlines was formed in the Pliocene Epoch; the second row including Tugulu, Manasi, Huoerguosi anticlines, was formed from the late Pliocene to the early Pleistocene; and the third row including Hutubi, Anjihai, Dusbanzi anticlines, was formed from early Pliocene to middle Pleistocene (Deng et al., 1999; Yu et al., 2012). Thrust and fold structures of basement-involved styles are developed in the first row, and detachment fold structures are formed from the second row to the third row (Fig. 1C). The factors controlling the deformation of structures have been simulated by sand-box experiment(Yu et al., 2009). The physical simulation results indicate that the orthogonal compression coming from Bogeda Mountain and the oblique compression with

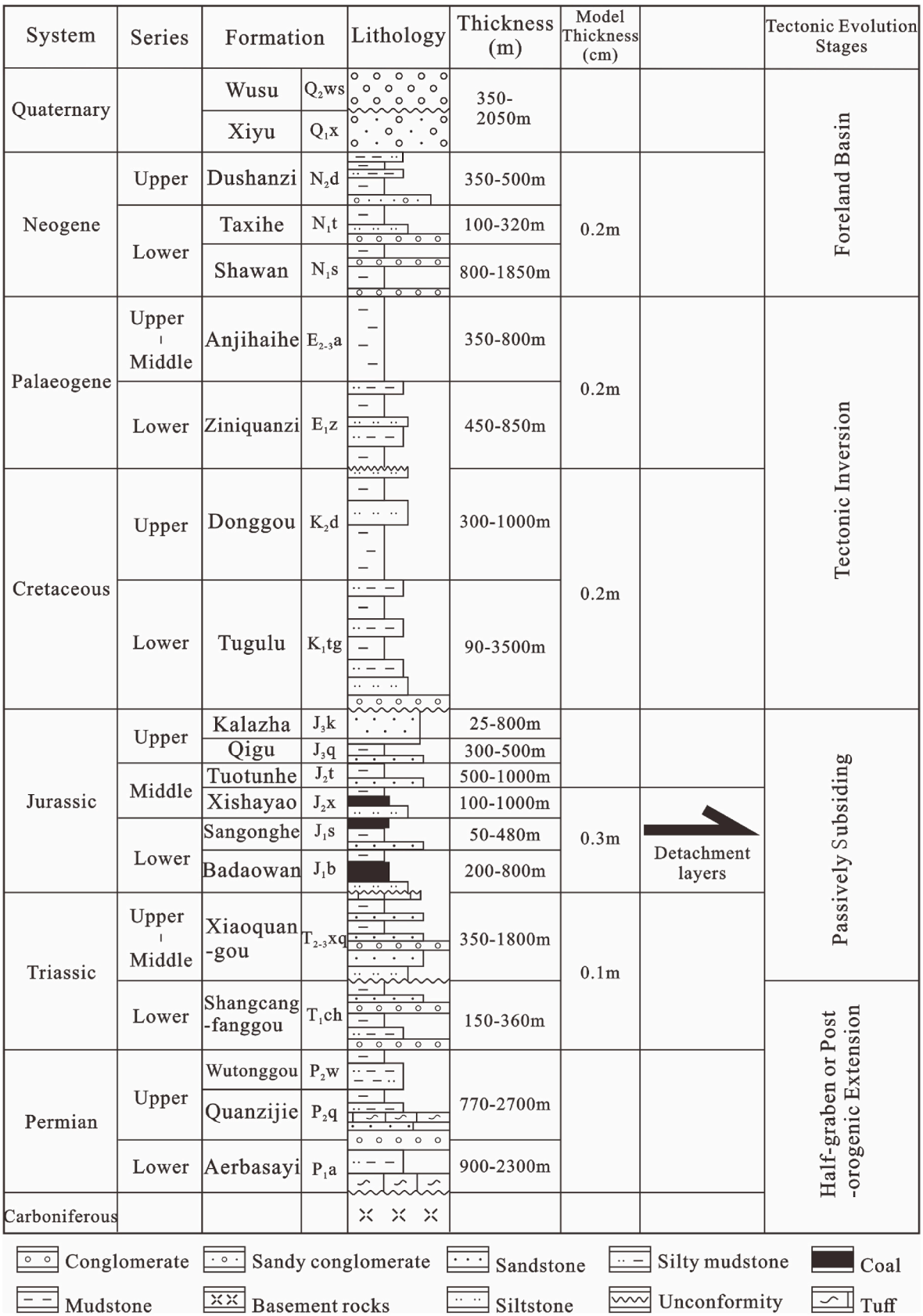

Fig. 2. Simplified litho-stratigraphic chart of the southern margin of Junggar Basin (modified from Ma et al., 2019).

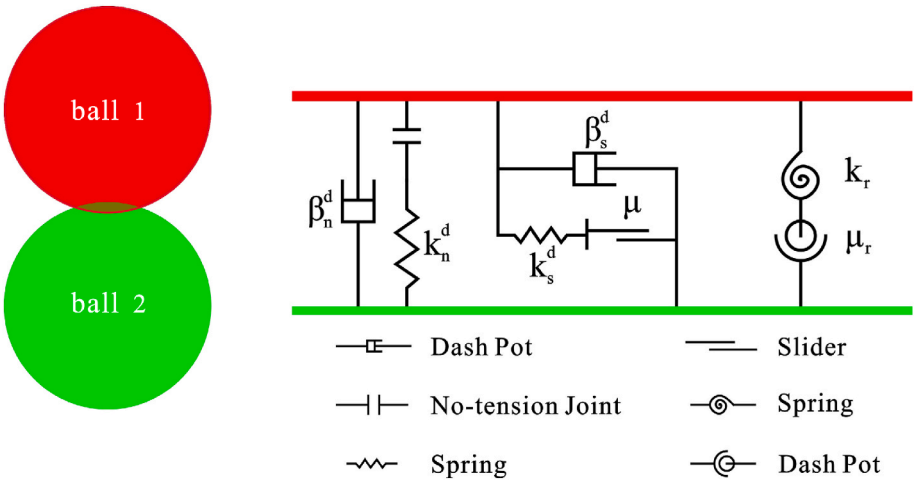

Fig. 3. Behavior and rheological components of the rolling resistance contact model in discrete element model.

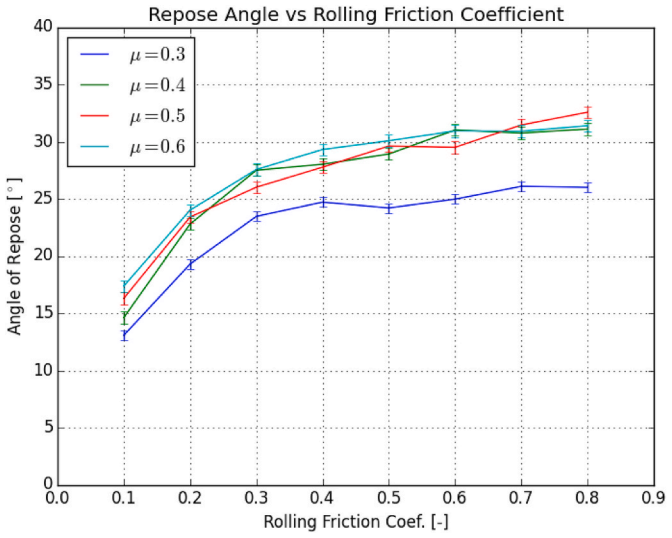

Fig. 4. The geometry of the heap showed by angle-of-repose versus rolling friction coefficient μ_r.

an angle of 75° between the stress and the boundary originating from the North Tianshan in the Cenozoic Era were responsible for the deformation differences between the eastern and the western part (Fu et al., 2003; Yu et al., 2009; Ma et al., 2019). However, due to the limitation of analogue experiments, transport of material along the transfer faults during the process of thrusting have not been well descripted in previous studies. Because the physical simulation can only provide the final results to cut sections, we cannot get the instantaneous information of the internal deformation during the modelling process, and do not know how the transfer faults link the fold-and-thrust sub-segments in the back piedmont and the deformation front..

The discrete-element method (DEM) is advantageous for the reconstruction of small-scale structures in the upper crust (Gray et al., 2014; Zhou et al., 2019).The formation process of accretionary wedges, including material stacking and rotation, are investigated in two-dimensional (2D) numerical simulations (Dean et al., 2013; Wenk and Huhn, 2013; Wang et al., 2019). Three-dimensional (3D) numerical models have rarely been used to study the structural evolution and material transport under the differential shortening conditions (Furuichi et al., 2018). Thus, we designed two 3D discrete-element simulations in order to investigate the evolution of the internal structure and material transport among the four velocity modules. In the end, we compared the simulation results with the fold and thrust belts developed in the northern margin of the Tianshan mountains. The study results can be used to analyze the development of the petroleum traps in the similar areas with compressional deformation..

2. Simulation method

Comparing to physical analogue experiment, DEM numerical simulation can save the results of each step during deformation, and the simulation can be sliced cross every direction for detailed deformation process. Furthermore, particles in each saved simulating results can display various properties, such as position, displacement and instantaneous velocity in three-dimensional space. With such information from DEM simulations, we can get access to the kinematic mechanism of tectonic deformation more effectively. The DEM is widely used in geotechnics simulations (Ai et al., 2011), and the results are similar to those of sandbox experiments and to those observed in nature (Abe et al., 2011). The DEM can handle more detailed structural deformation than a finite-element simulation (Zhang et al., 2013). A DEM simulation is about the movement and interaction of particles that obey Newtonian dynamics (Cundall and Strack, 1983). Balls, walls and the contact model are the required components of particle flow. Once the initial conditions are set, the granular behavior evolves according to the physics coded into the simulation (Saltzer and Pollard, 1992; Hazzard and Mair, 2003; Potyondy and Cundall, 2004; Abe et al., 2011). To achieve the more similar macroscopic deformations, the properties of granular materials and the contact model must be carefully selected; in this work, we use the linear rolling resistance model, which is based on the linear model (Iwashita and Oda, 1998; Ai et al., 2011). This contact model not only uses spring and damper interaction between particles but also takes the rotation of the particles into consideration (Iwashita and Oda, 1998; Ai et al., 2011; Zhou et al., 2013; Jiang et al., 2015). In this study, the

Table 1
Macroscopic properties of DEM particles in simulations.

	Granular Size (cm)	Density (kg/m^3)	Porosity	Emod (Pa)	Internal friction	Rolling resistance	Bond gap (cm)
Frictional material	3.5 ± 0.875	2600	0.37	2×10^8	0.6	0.1	–
Ductile material	3.5 ± 0.875	2600	0.37	0.3×10^8	0.5	0.01	5×10^{-3}

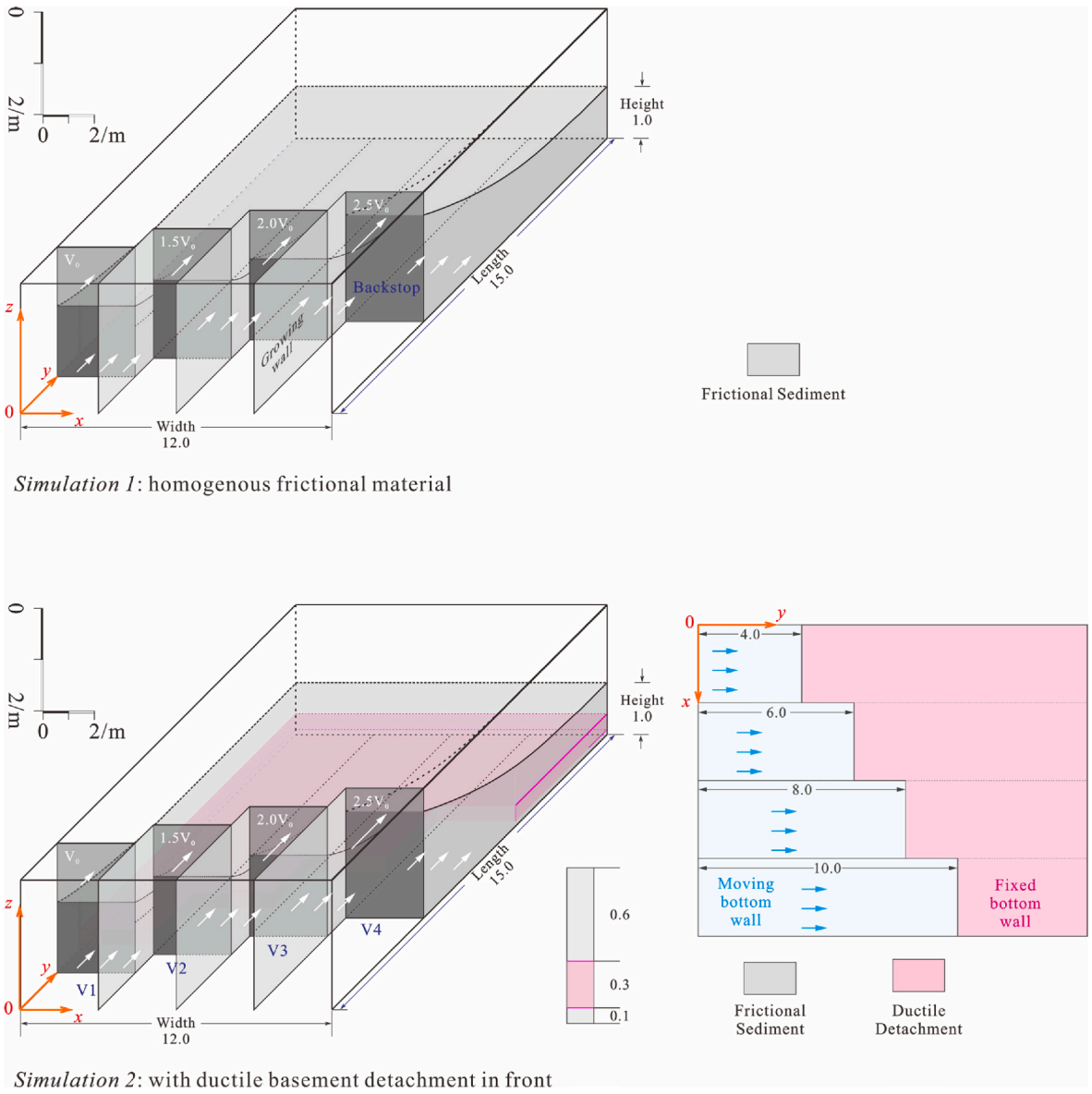

Fig. 5. Schematic drawings of the two simulations and their simulating stratum setting. Simulation 1 is a differential contraction DEM simulation with homogenous frictional material. Simulation 2 is a differential contraction DEM simulation with ductile substrate in front of the contraction range.

simulation experiments are computed by the software called 3D Particle Flow Code (PFC^{3D}).

The contact force (Fc) between two balls, or between a ball and a wall combines linear force (Fl), a dashpot force (Fd) and rolling friction torque (Mr) (Ai et al., 2011), and no tension exists in the contact (Fig. 3). When the gap between two objects is less than or equal to zero, the contact model is activated. This model includes an elastic rotational spring, a dash pot, a non-tension joint and a slider (Fig. 3), and the relative rotation between particles strongly affects the shear bond (Ai et al., 2011).

The key parameters for the rolling-resistance contact model are as follows: (1) linear force can be divided into normal and shear components, Fl n and Fl s, which are produced by the constant normal and shear stiffness kl n and kl s. The slip is accompanied by a shear force that is related to the internal friction coefficient μ. (2) The dashpot force also has normal and shear components, Fd n Fd s, and normal and shear critical-damping, βd n and βd s, control the associated forces. (3) Rolling-friction torque depends on the rolling stiffness k_r and is limited by the rolling resistance coefficient μ_r.

3. Model setting

3.1. Simulation material

Dry quartz sand is a conventional Mohr–Coulomb material that is widely used to simulate the deformation of the upper crust (McClay, 1990; Dooley et al., 1999; Gray et al., 2014). Mesoscopic particles are closely associated with macroscopic structural deformation in nature (Groshong Jr, 1994; Potyondy and Cundall, 2004; Abe et al., 2011). The friction angle φ of dry quartz sand is approximately 30° (van Gent et al., 2010), so the $\mu = \tan \varphi$ gives $\mu = 0.577$. However, this result holds only for natural particles and not for numerically simulated particles. Since the development of the contact model, the parameters in 2D simulations can be mirrored to 3D (Furuichi et al., 2018). Angle-of-repose tests show that, given internal friction coefficients of 0.2, 0.1, and 0.05, the angles of repose of the bulk material are 30°, 20°, and 10°, respectively (Hardy et al., 2009). When $\mu = 0.3$, more accretionary wedge-deformation DEM simulation results are closer to physical analog models (Li, 2019) in no-rolling-resistance situations. The bulk material properties are verified through the use of three-dimensional angle-of-repose experiments.

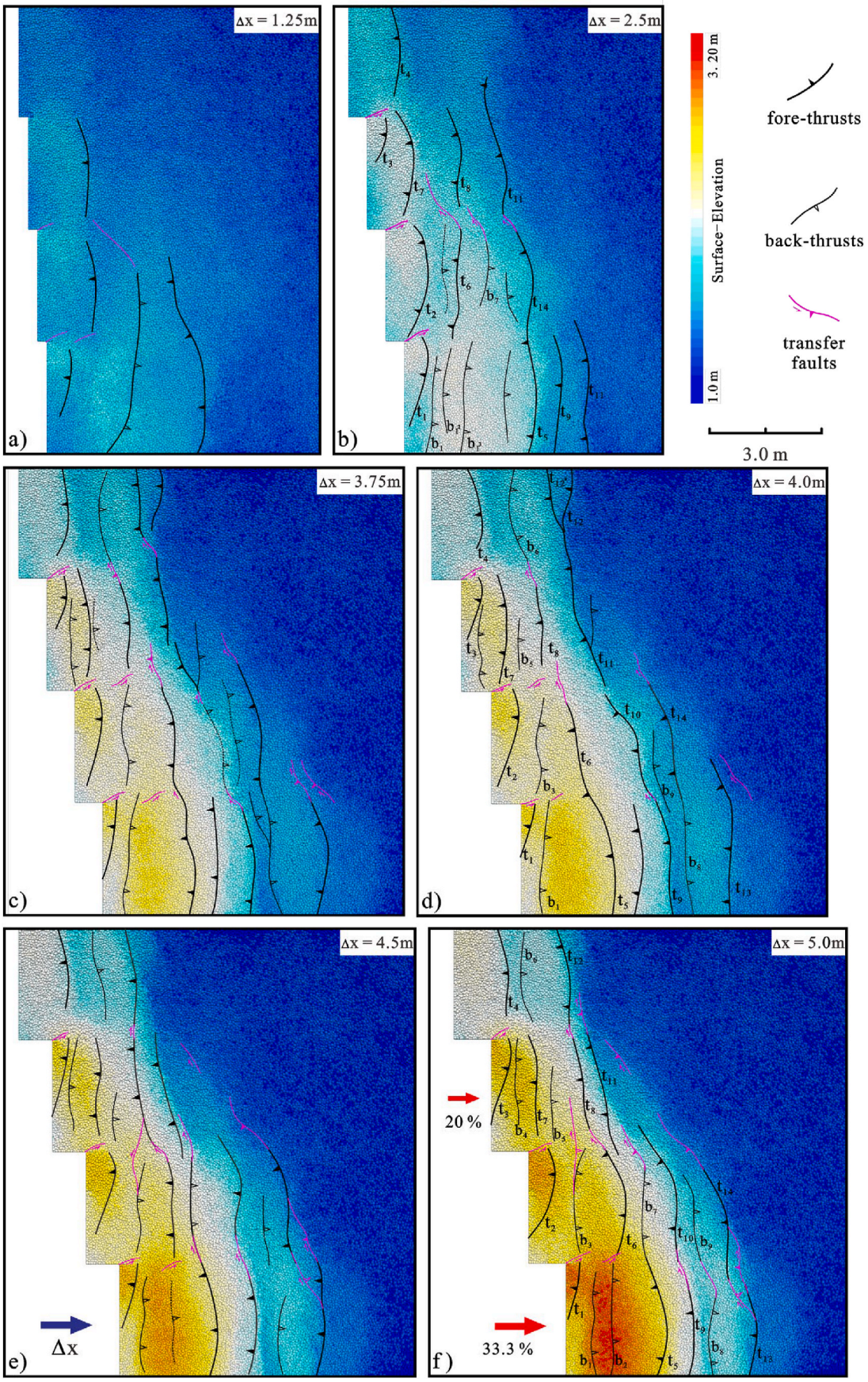

Fig. 6. Topography of Homogenous Simulation showing the fault propagation as shortening. Shortening of V4 module is given in the top right-hand corner of the pictures. All thrusts are numbered, t represents frontal thrust and b represents back-thrust.

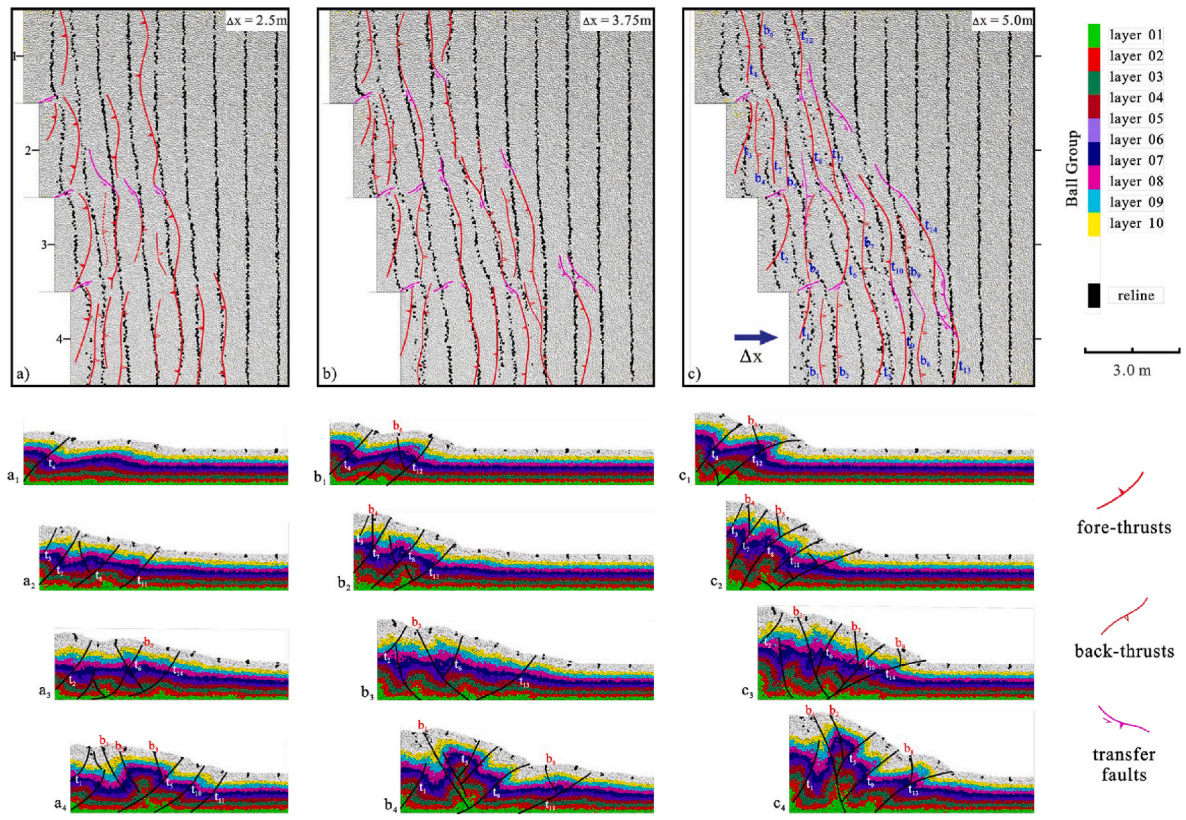

Fig. 7. Structural interpretation of the fault patterns in the Homogenous Simulation from a series of top views, and vertical cross-sections parallel to the shortening direction (with subscript). a) 16.67% shortening in V4 module; b) 25.0% shortening in V4 module; c) 33.33% shortening in V4 module. The ball group is distinguished by different colors and the black lines in map view are the reference lines, which facilitate fault identification. (For interpretation of the references to color in this figure legend, the reader is referred to the Web version of this article.)

On the location of the balls that are recognized on the free surface of the heap. The dip angle of the cone surface is practically the repose angle. This procedure was repeated 32 times with varying values of μ_r from 0.1 to 0.8 in an increment of 0.1 and μ from 0.3 to 0.6 in an increment of 0.1. Therefore, we built the relationship between the μ_r and the repose angle. Under the rolling resistance contact model, the repose angle corresponds to the crustal sediments (30°) when the μ is 0.6, μ_r is 0.5 (Fig. 4).

The macroscopic material parameters used herein in DEM simulations are based on repeated angle-of-repose experiments using the rolling resistance contact model (see Table 1). The brittle simulating stratum (the density is 2600 kg/m^3; granular size is 3.5 ± 0.875 cm; Young's modulus is 2×10^8 Pa; coefficient of internal friction is 0.6; μ_r is 0.5, and both normal and shear damping coefficients are 0.2) simulates clastic rocks in nature and corresponds to dry quartz sand in sandbox experiments. These particles consist of brittle simulating stratum that adheres to the Mohr–Coulomb failure criterion. To simulate the rocks under high confining stress, the ductile materials have lower friction (μ is 0.1) and lower stiffness (Young's modulus is 0.3×10^8 Pa), which increases deformability (Kh et al., 2011). In addition, the bond gap is defined between the particles of ductile materials to simulate viscous behavior.

3.2. Model setup and kinematics

Despite the computational cost, a 3D simulation can provide more comprehensive results than sectional deformation in 2D models (Ruh et al., 2014). The evolution of the structural style from the top view is necessary in this research in order to observe the deformation of transfer zones. Therefore, two 3D DEM simulations follow the same movement process but comprise different simulating stratums, they were conducted to study the structural evolution under differential compression and to analyze the effect of ductile basements on deformation patterns. The two simulations are 12.0 m wide in the *x* direction, 15.0 m long in the *y* direction, and 3.0 m tall in the *z* direction, and the particles are generated within this domain (Fig. 5).

The four modules are divided evenly in the *x* direction, and each consists of a mobile backstop wall, a moving bottom wall, and a fixed bottom wall. Each module is 3.0 m wide and 15.0 m long. All mobile backstop walls move parallel to the *y* direction but at different constant velocities: 0.01 m/s for module V1, 0.015 m/s for module V2, 0.02 m/s for module V3, and 0.025 m/s for module V4. The compressional velocity has little influence on the development of structural patterns (Ruh et al., 2014). We applied the same convergence velocity of each mobile backstop to the moving bottom walls, and the fixed bottom walls are stationary.

Due to the different velocity, the lengths of the moving bottom walls differ in the four modules (4.0, 6.0, 8.0, and 10.0 m, respectively). The lengths of the fixed walls are 11.0, 9.0, 7.0, and 5.0 m, respectively. To minimize the boundary effect, the side walls should be as smooth as possible, which corresponds to smooth glass in sandbox experiments (Hazzard and Mair, 2003; Bonnet et al., 2007; Taniyama, 2011; Jiang et al., 2015; Chemenda et al., 2016; Sun et al., 2016) (the internal friction coefficient is 0.01). The bottom walls require greater friction (the internal friction coefficient is 0.6) to drive the upper simulating stratum.

During later movement, the gap between the backstops increases, so walls are grown along the compression direction to ensure the closure of the model. In both simulations, the initial area filled with particles is 12.0 m × 15.0 m × 3.0 m. Simulation 1 (homogeneous simulation) fills the area with homogenous brittle sediment, and simulation 2 (detachment simulation) places a ductile detachment above the same area of fixed walls. The thickness is 0.3 m with 0.1 m brittle material below and

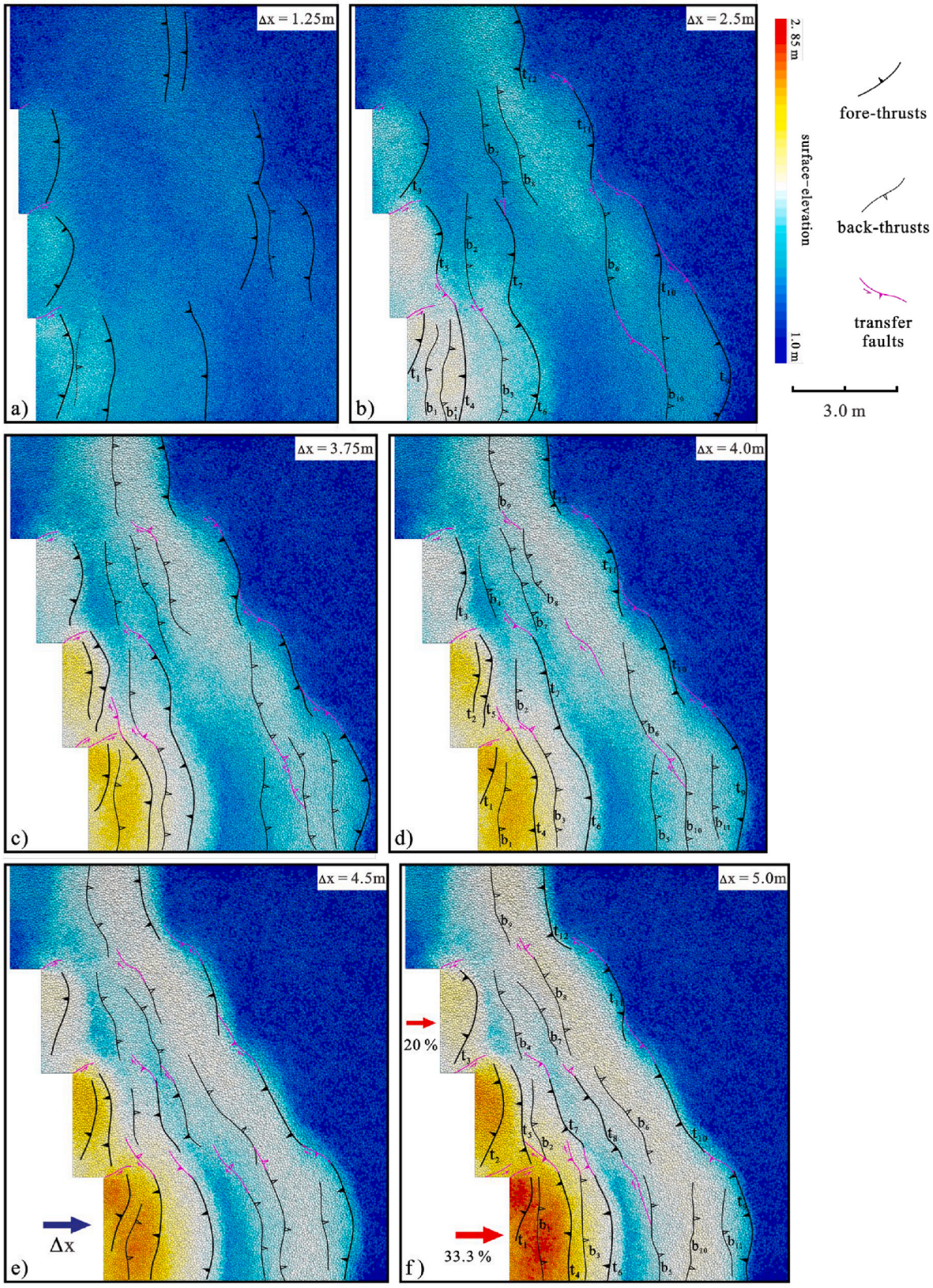

Fig. 8. Topography of Ductile Detachment Simulation showing the fault propagation as shortening. Shortening of V4 module is given in the top right-hand corner of the pictures. All thrusts are numbered, t represents frontal thrust and b represents back-thrust.

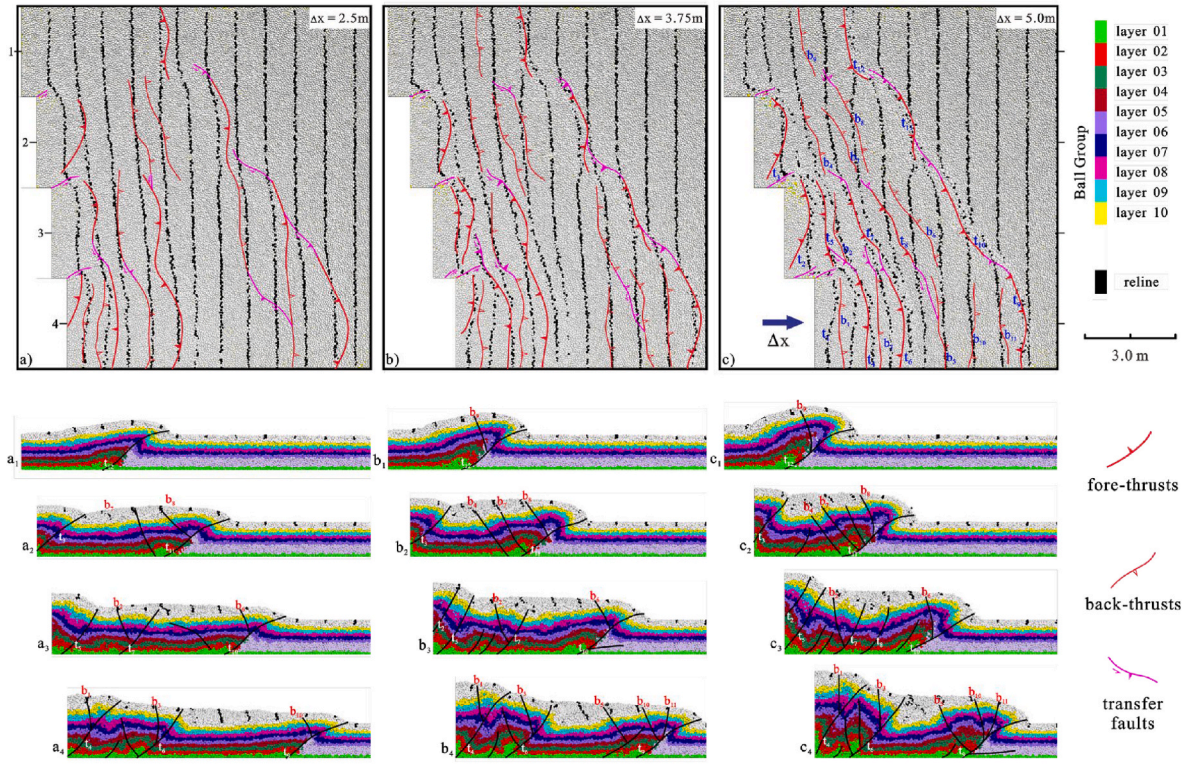

Fig. 9. Structural interpretation of the fault patterns in the Ductile Detachment Simulation from a series of top views, and vertical cross-sections parallel to the shortening direction (with subscript). a) 16.67% shortening in V4 module; b) 25.0% shortening in V4 module; c) 33.33% shortening in V4 module. The ball group is distinguished by different colors and the black lines in map view are the reference lines, which facilitate fault identification. (For interpretation of the references to color in this figure legend, the reader is referred to the Web version of this article.)

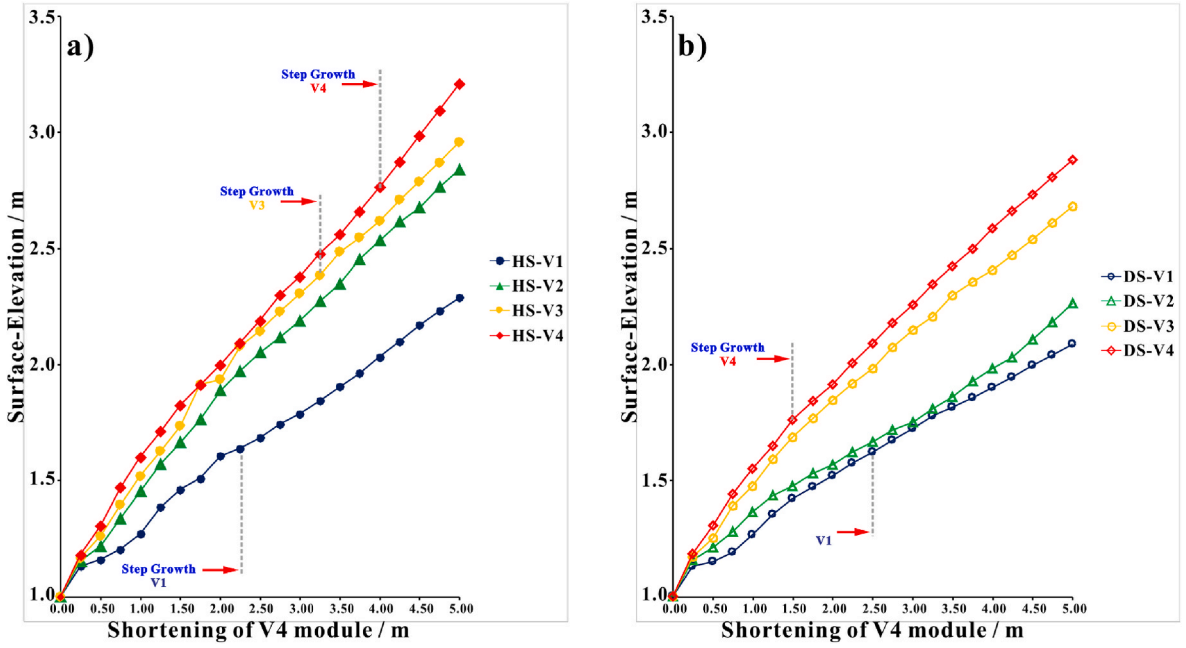

Fig. 10. Surface-elevation measurements taken from the simulations during the shortening. a) Homogenous Simulation with solid points; b) Detachment Simulation with hollow points.

0.6 m brittle material above (Fig. 5). Ten sub-layers whose thickness is 0.1 m are chopped up and shown in different colors to facilitate viewing of the deformation. Only specific walls move at constant velocity; all particles are initially at rest.

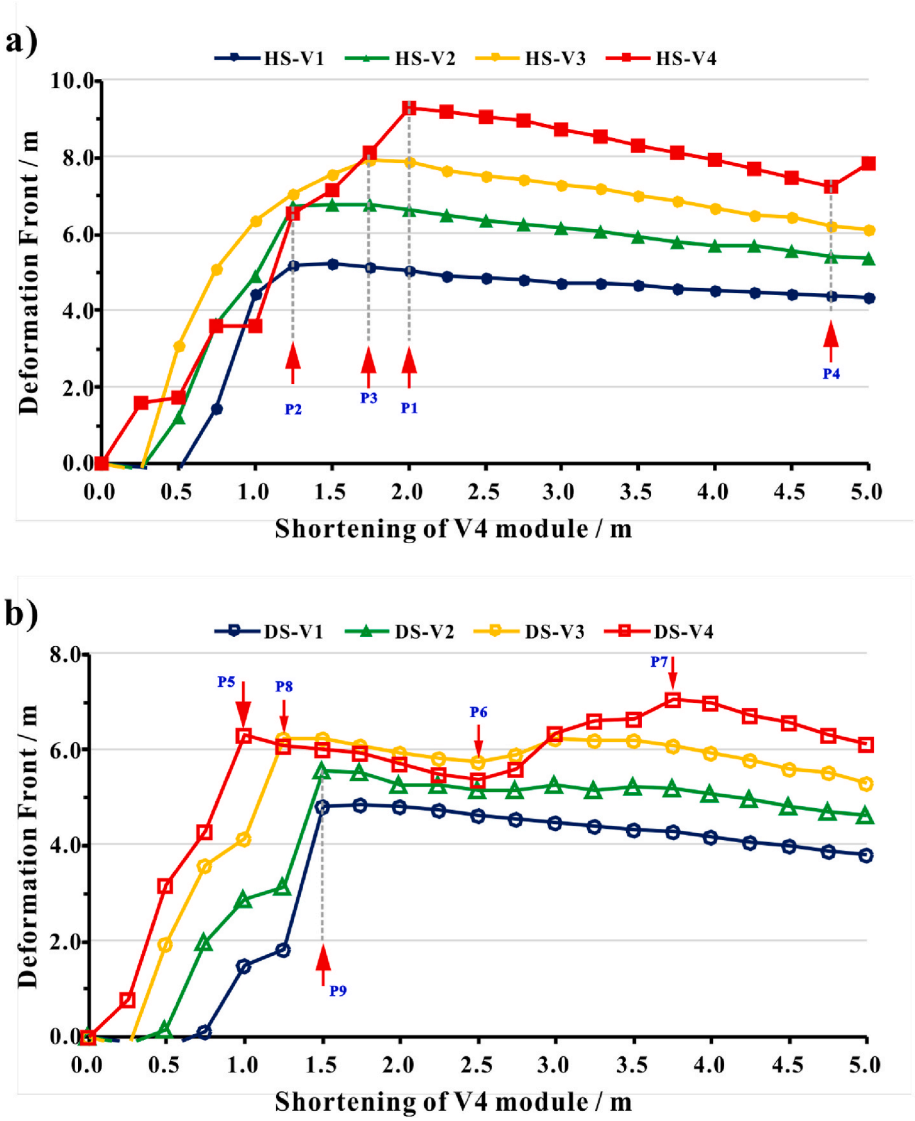

Fig. 11. Deformation front curves measured from each velocity module of differential compression simulation. a) Homogenous Simulation with solid points; b) Detachment Simulation with hollow points. The nucleating process of the tectonic wedges is characterized by rapid propagation rate, and slow growth suggests the wedge movement after nucleation.

4. Results

4.1. Differential compression DEM simulation with homogenous brittle sediments

The decrease in velocity creates different compressional bulks for each velocity module at the same time. As a sequence, structural patterns in each velocity module can interact with neighboring ones, which can be interpreted and illustrated by the plan (Fig. 6) and the cross-sections (Fig. 7) of the simulations. In the homogenous simulation, the deformation of each velocity module takes the form of a basic wedge that develops with zero basal decollement (dip β). This simulation is designed to investigate the deformation of homogenous frictional sediments. The thrusts first appear in module V4, and back-thrust occurs at 8.33% shortening, they form the pop-up structure together. Relatively low compression only produces thrusts that die out in the neighboring velocity modules (Figs. 6a, 7a and 7b and 7c).

A flat-topped, symmetrical anticline forms in the V4 module when the shortening reaches 2.5m (Fig. 7b). As the shortening accumulates, the thrusts nucleate in front of the backstop of module V4, and the frontal anticline becomes asymmetric with stronger back-thrusts than fore-thrusts. Back-thrusts are well developed in the other three slower modules. Three rows of anticlines appear in module V3; they develop from a large ramp-flat thrust (t_6, t_{10}, t_{14}) and a secondary back-thrust (b_3, b_7, b_9). In addition, clockwise rotation is the main reason that listric faults develop into the ramp-flat fault (Fig. 7c_3). Out-of-sequence trust t_{10} results in imbrication with t_5 and t_{14}(Fig. 7b_3 to 7c_3), which convert shortening to displacement along the new thrust.

Two types of transfer zones develop in the differential compression simulation at domains adjacent to the faster backstops and between the deformation front. Riedel shear is generated on the slower side of two adjacent modules, and the thrusts confined to each module terminate at the Riedel shear. The difference in topography between Riedel shears is also a magnified sign of fracture (Fig. 6f). The other type of transfer faults links the thrusts between two neighboring modules at the deformation front and are generally oblique relative to the shortening direction. Through this oblique structure, curved fold-and-thrust belts thrive in the simulation and also appear in adjacent rheological sediment, basement setting, substantial topographic relief and the geometry of backstops.

As the shortening increases, the thrusts of the fast module produce greater displacement in the direction of compression than those in

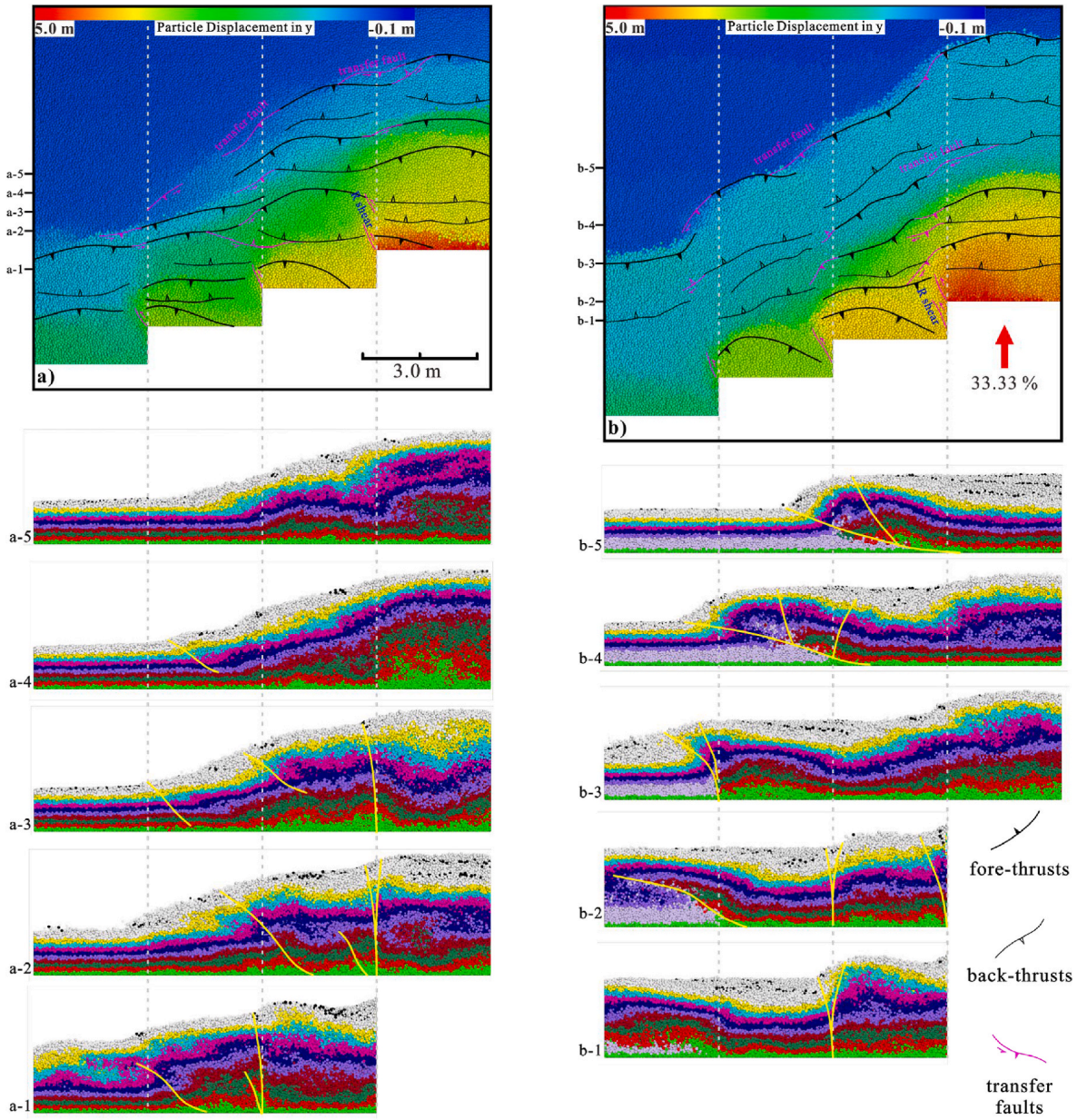

Fig. 12. Particle displacement in shortening direction. a) The final stage of Homogenous Simulation; b) The final stage of Detachment Simulation. Structural styles of the transfer faults are illustrated by the cross sections perpendicular to the shortening direction. Section locations are shown in the upper pictures.

adjacent slower modules, which leads to the separation of heretofore connected faults t_5 and t_6 (Fig. 6d). A new link connects to the thrust (or back-thrust b_7) further ahead (Fig. 6f). Dip changing along the fault strike is one evident feature of strike-slip faults; the forward-vergent thrust t_5 in module V4 (Fig. 6f) links with the rearward-vergent back-thrust b_7 in module V3 (Fig. 6f) via a strike-slip fault (in pink), which belongs to the frontal transfer zone.

4.2. *Differential compression DEM simulation with ductile detachment*

The ductile layers in the four modules are set according to the shortening of each module. The V1 module compress faster and farther. Thus, the ductile detachment is set close to the end wall. On the contrary, the ductile detachment of the slower modules is set close to the moving backstop. Deformation prefers the incompetent layers (Reiter et al., 2011; Ruh et al., 2013, 2014; Wu et al., 2014; Borderie et al., 2018), so thrusts occur simultaneously near the backstops and above the detachment, except in module V4 for which the backstop is well separated from the detachment distributed range under insufficient shortening (Fig. 8a).

In-sequence imbricate thrusts near the backstops are inconspicuous, which is characteristic of nucleates, unlike the situation for the homogenous simulation. In contrast, the pop-up structure generated by ramp-flat thrusts below and back-thrusts appears above the thick ductile layer border (Fig. 9). As two rows of anticline develop, a relatively low border and flat sag develop between them without faults (Fig. 9b_3 and 9b_4) is narrowing along with the compression. Out-of-sequence thrusting in ductile detachment simulation (Fig. 9b_3 to 9c_3) is significantly influenced by ramp-flat thrust developing above the detachment layer. T8 occurs after thrust t7 but after t10, can be seen as in-sequence thrusting in piedmont thrust belt and out-of-sequence thrusting in the whole study area.

Riedel shears form relatively poorly at the foot of moving backstops, so only incomplete fractures rooted at the growing walls on the slower side appear after the compression (Fig. 8). Conversely, strike-slip faults belonging to the frontal transfer zone represent stronger activity with a

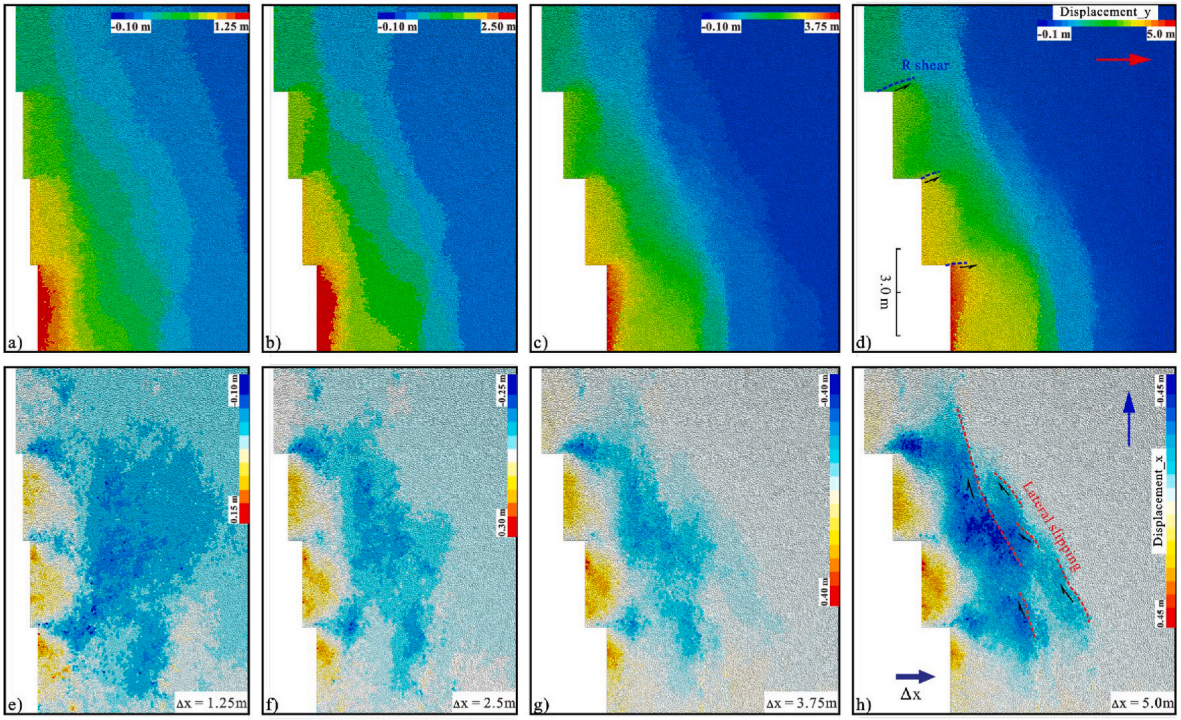

Fig.13. Overview of material transportation evolution in shortening direction and lateral migration of Homogenous Simulation. The interpretation of R shears is based on the offset in movement direction and transfer faults in front of the wedge are recognized by the offset in lateral direction.

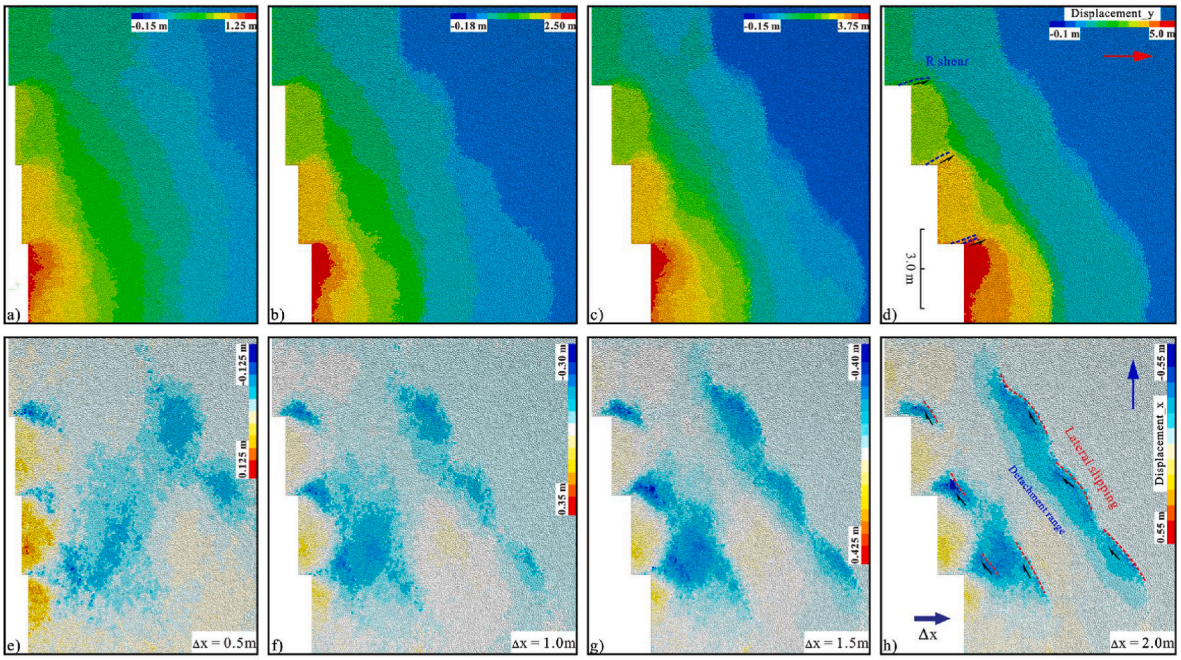

Fig. 14. Overview of material transportation evolution in shortening direction and lateral migration of Detachment Simulation. The interpretation of R shears is based on the offset in movement direction and transfer faults in front of the wedge are recognized by the offset in lateral direction.

higher degree of transfer obliquely to the thrusts and a greater scale of linkage between the two compressional faults of the two velocity modules. The thrusting structures into the two velocity modules do not separate during compression because the convergence is accommodated by two structural belts rather being concentrated in one fold-and-thrust belt. Compression at the ductile detachment border is reflected in the propagation of the back-thrusts (Fig. 9c_2) and the developing stack of pop-up structures (Fig. 9c_2 and 9c_4).

4.3. Evolution of orogenic wedges in each velocity module of differential compression simulation

Based on the critical taper theory, under-plating and subsequent uplifting are the mechanisms that cause the wedges to grow (Willett, 1992; Cotton and Koyi, 2000; Bonnet et al., 2007; Graveleau et al., 2012; Wenk and Huhn, 2013). In this work, we used displacement measurements to quantify the granules' trajectory by investigating the

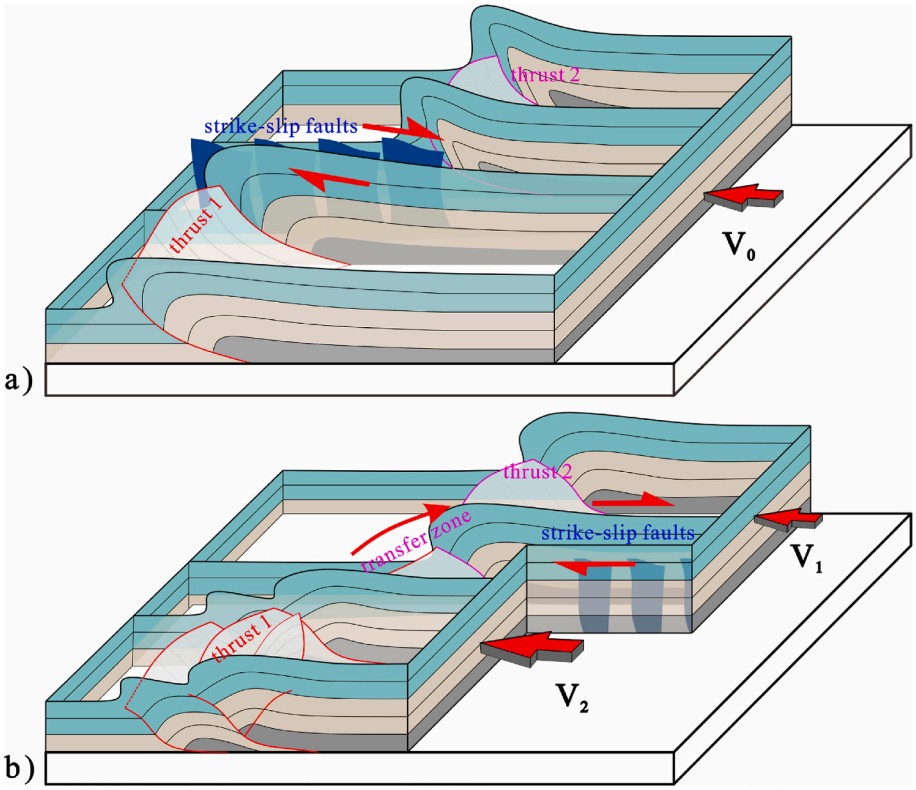

Fig. 15. Schematic diagrams illustrating the location of tear fault zone, (a) one model modified from Fossen (2016) and (b) the model based on the results of this research.

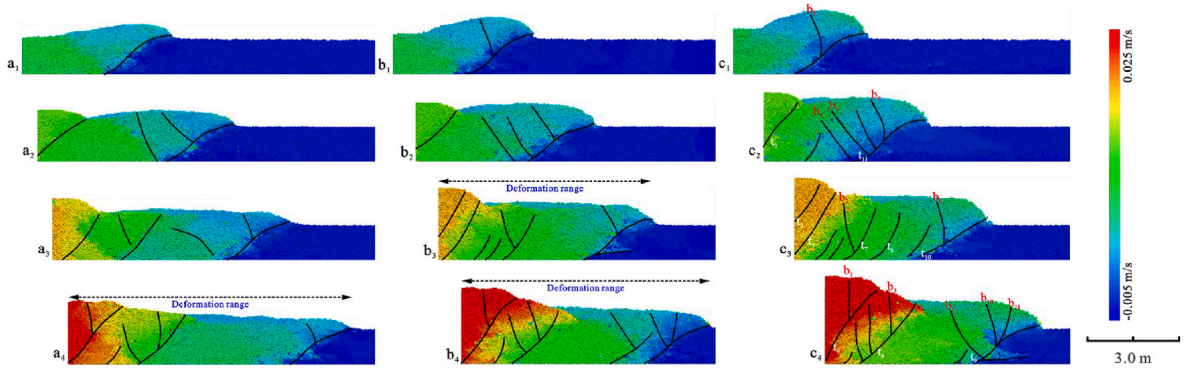

Fig. 16. Temporal velocity filed of particles in Detachment Simulation during the simulation. a: 16.67% shortening in V4 module; b: 25.0% shortening in V4 module; c: 33.33% shortening in V4 module. The section locations are the same as that in Fig. 8

propagation of wedges in each velocity module under the influence of drag from the adjacent module in differential compression simulations.

Surface elevation can reflect the under-plating movement of particles during the shortening (Willett, 1992; Graveleau et al., 2012; Wenk and Huhn, 2013). Deformation propagates farther above the incompetent ductile detachments, which are set at the frontal, longer shortening range in ductile detachment simulation absorbs the same shortening bulk than the homogenous simulation. Therefore, shorter wedges in each module appear in the detachment simulation (Fig. 10b). The "step" growth tendency during the orogen wedge propagation signals the change of the uplift and compression due to the wedge locomotion, which is related to the development of new thrusts. This characteristic is more evident in module V1 of the homogenous simulation (Figs. 10a and 7) due to the more active inception of new foreland-vergent thrusts.

In this work, the location of the deformation front is recorded from the backstop wall, and the two stages in these two simulation results are (i) the process of wedge formation, nucleating in priority, and (ii) the compression of the wedge in priority. Before point P2 (Fig. 11a), imbricate fans of in-sequence thrusts are well developed, with each rapid propagation corresponding to a new thrust. As shortening, new thrust t_{13} (Fig. 7b$_4$) occurs at the same time as the wedge enveloped within thrust t_{11} is compressed, which happens between points P2 and P1. Continuous nucleation of the wedge of module V4 continues to the point P4, where a new fore-land thrust forms. Other modules have a similar growth pattern, which indicates the similarity of the evolution of the fold-and-thrust belts under the different compression velocities. Deformation in module V3 is affected by both fast and slow modules because of frictional resistance behavior particles (Aridhi et al., 2014). Inconspicuous nucleating features are caused by the foregoing thrust in module V4, and the effects of drag from the slower adjacent module lead to the unusual development of back-thrusts.

A more complicated growth process occurs in the detachment

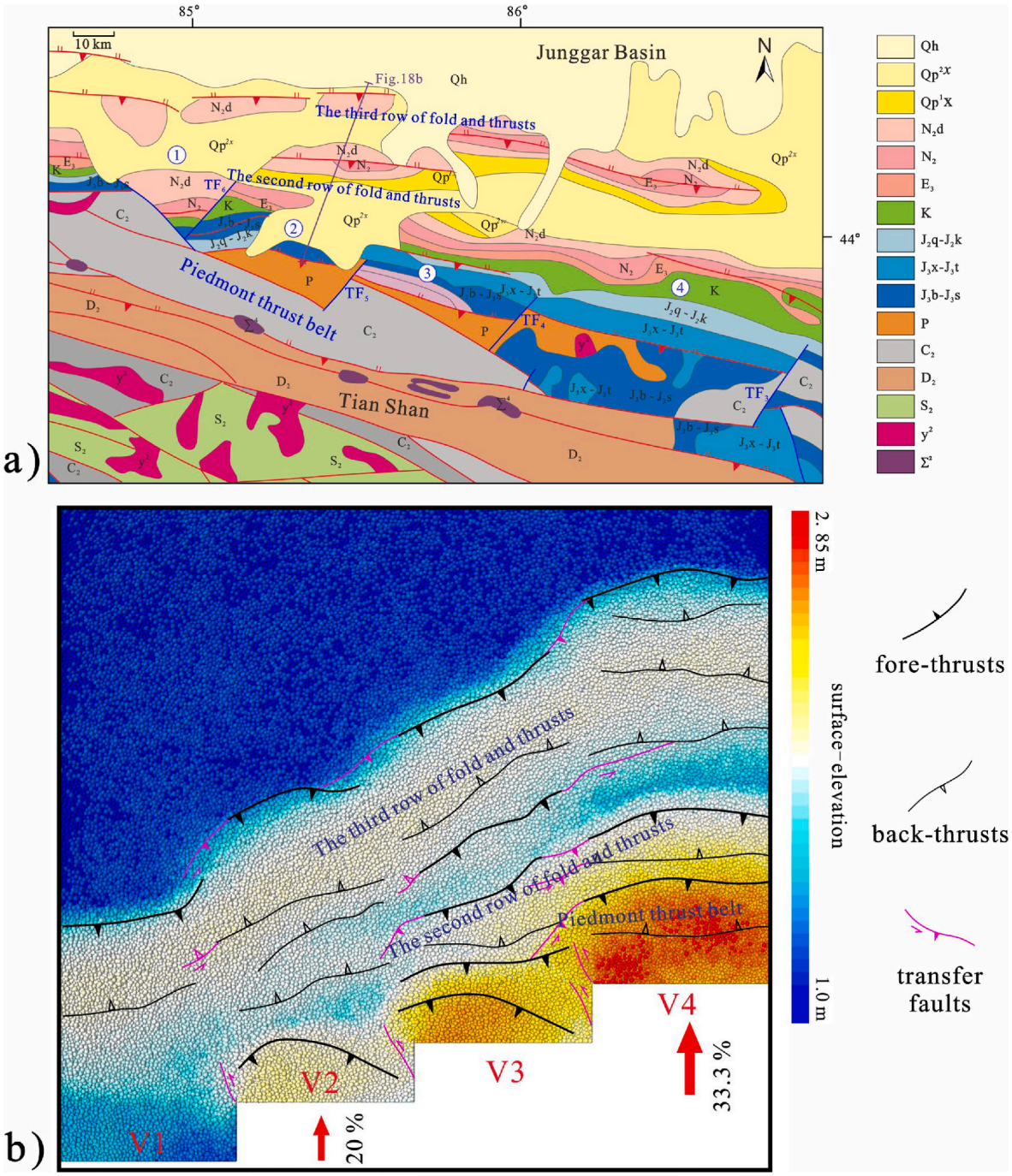

Fig. 17. Comparison between the a) simulation result from the top view and b) topographic map of the western segment in the Southern Margin of the Junggar Basin (adapted from Shengli Oilfield) which is characterized by oblique anticlines.

simulation due to the existence of the deformation preference detachment layer, which would destroy the integrated formation of the wedge; in other words, no nucleating is apparent. Before points P9, P8, and P5, thrusts develop only at the toe of the backstops in each module, and beyond these points are formed low-angle ramp-flat thrusts reaching the ductile detachments. Compression of the simulated sediment occurs in the undeformed range from the box-fold (Fig. 9b) to the front of the detachment until point P6, and then the accumulation of shortening is accommodated through the development of back-thrusts. And then, the deformation front increases slowly in this place.

5. Discussion

5.1. Strike-slip systems in differential-shortening simulations

Faults patterns and their evolution of two types of transfer zones have been described in plan view (Figs.12 and 13). In addition, the sections that cut across the shear faults differ significantly from each other. Riedel shears in front of the backstops are characterized by steep faults, which are more active and display a “flower” structure in the slower module (Fig. 12a-1). However, in the faster module the thrusts faults show as low angle reverse faults (Fig. 12b-2). Curved strike-slips faults, which serve as links between the thrusts in two adjacent modules, show a low angle thrust rooting down to the bottom of the faster

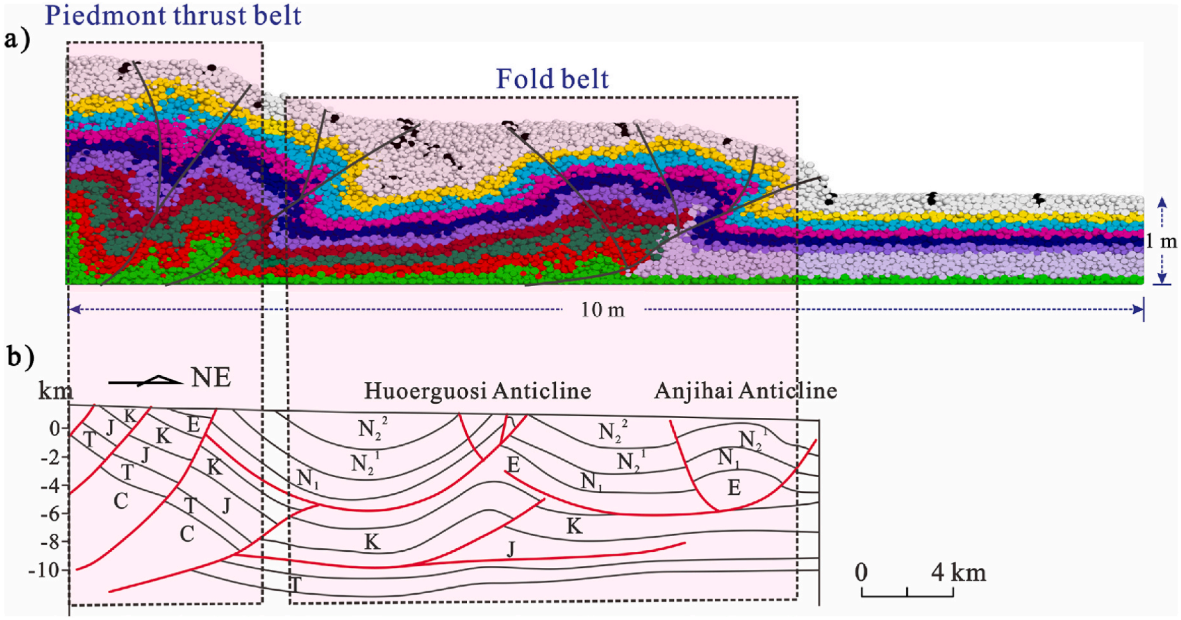

Fig. 18. Comparison between the simulation section and the interpreted seismic profile. a) Cross-section across to the middle of the fastest velocity module and b) Cross section (see location in Fig.16a) showing Huoerguosi and Anjihai anticlines (from Yu et al., 2012).

module (Calassou et al., 1993; Ruh et al., 2013). Especially in the ductile detachment simulation, folds in the hangingwall are uplifted by the smooth trajectory thrust that slides along the detachment of slower module and the branch back-thrusts, and particles in the footwall are more static (Fig. 12b–2 and 12b-4). These results are similar to those cases found by physical analog models (Calassou et al., 1993) and finite difference method (Ruh et al., 2014) (see Fig. 13).

In this work, we use material transportation to illustrate the evolution of the two types of transfer zones and the curved fold-and-thrust belts (Figs. 13 and 14), which are achieved by tracing particle displacement in both the shortening and lateral directions. Strike-slip faults to the foreland suggest that the lateral material transportation is affected by the high shortening rate of the faster module (Reiter et al., 2011). Two transfer-fault-breaking processes are recognized in the course of the differential compression simulation: (1) Thrusts in the faster module grow quicker than those in the slower module before nucleation finishes (see b_2 and b_3 in Fig. 8b and d). (2) After the first nucleation of the wedge, it uplifts vertically as a whole, creating new thrusts that form the deformation front. Nevertheless, particles in the slower module still move with significant shortening displacement, and the thrusts in the slower module can connect through the transfer fault with new frontal thrusts in the neighboring module (see t_5 and t_{14} in Fig. 6b and f). The accumulation of differential strain leads to transfer faults at the deformation front.

Strike-slip faults that connect two parallel trusts faults are also found in the Alpujarras transfer zone (Martínez-Martínez et al., 2006). However, a major problem with this type of fault is whether contraction can propagate within the entire area from the moving backstop to the most frontal reverse fault. If there is no difference in material setting (Adam et al., 2005; Borderie et al., 2018) or pre-existing structures (Macedo and Marshak, 1999; Sun et al., 2016), the results of 3D physical sandbox experiments indicate that the deformation fronts appear nearly at the same distance from the backstops. In contrast, there is a doubt whether strike-slip faults would develop, and connect two parallel reverse faults under the same shortening (Fig. 15a). In recent years, an increasing amount of literatures discuss the lateral displacement accommodation that occurs in front of deformation front in slower intenders (Reiter et al., 2011) with velocity differential, same as produced by our models (Fig. 15b).

5.2. The role of thick viscous detachment

As the incompetent sediment material, the ductile detachment first deforms when the walls begin moving. Therefore, pop-up structures develop above ramp-flat thrusts that form in the decollement layer at the same time as do thrust belts near the backstops. A less active wide syncline sandwiched by two rows of thrust belts and structural patterns depends on the distance between the initial backstop position and the corresponding detachment border in the same module. The syncline appears gentler in module V4 than in the slower neighboring module. Shortening disperses in the entire deformation zone (Fig. 16), so a longer deformation range usually corresponds to lower uplifting and more lateral material transportation.

Cross sections of the temporal velocity field of the detachment simulation reveal the formation process of the structural pattern. The uplifting is related to the displacement increasing at a greater rate at the foot of the backstop, which reveals the under-plating mechanism of wedge growth (Fig. 16a_3 and 16a_4). The wedge is then characterized by the "triangular" shear zone closing to the backstop with a clockwise rotation, producing the hangingwall of the main thrust t_6, and relatively inactive particles in the footwall moving by a trapezoid. As shortening in faster module increases towards fixed walls from 25.0% to 33.33%, the displacement along the ramp-flat thrust t_9 produces another row of anticline forward (Fig. 16c_4). Ambiguous Riedel shears appear in detachment simulations and now thrusts occur in the two adjacent modules during the entire compression, which causes less difference in displacement. The different shortening distances concentrated near the backstops create Riedel shear (Naylor et al., 1986), following which the thrusts formed in front soon accommodate the compressive stress. This explains why the shear is limited to the toes of the backstops. Transfer faults that are oblique in front of the wedges transport material laterally. The uplifting of the hangingwall in the detachment simulation is characteristic of the ramp-flat fold sliding above the ductile detachment in the slower module. Material transportation in the shortening and lateral directions are the major kinematic mechanisms creating transfer faults in differential compression simulations.

5.3. Comparison with the southern margin of the Junggar Basin

The ductile detachment simulation results in plan view can compare

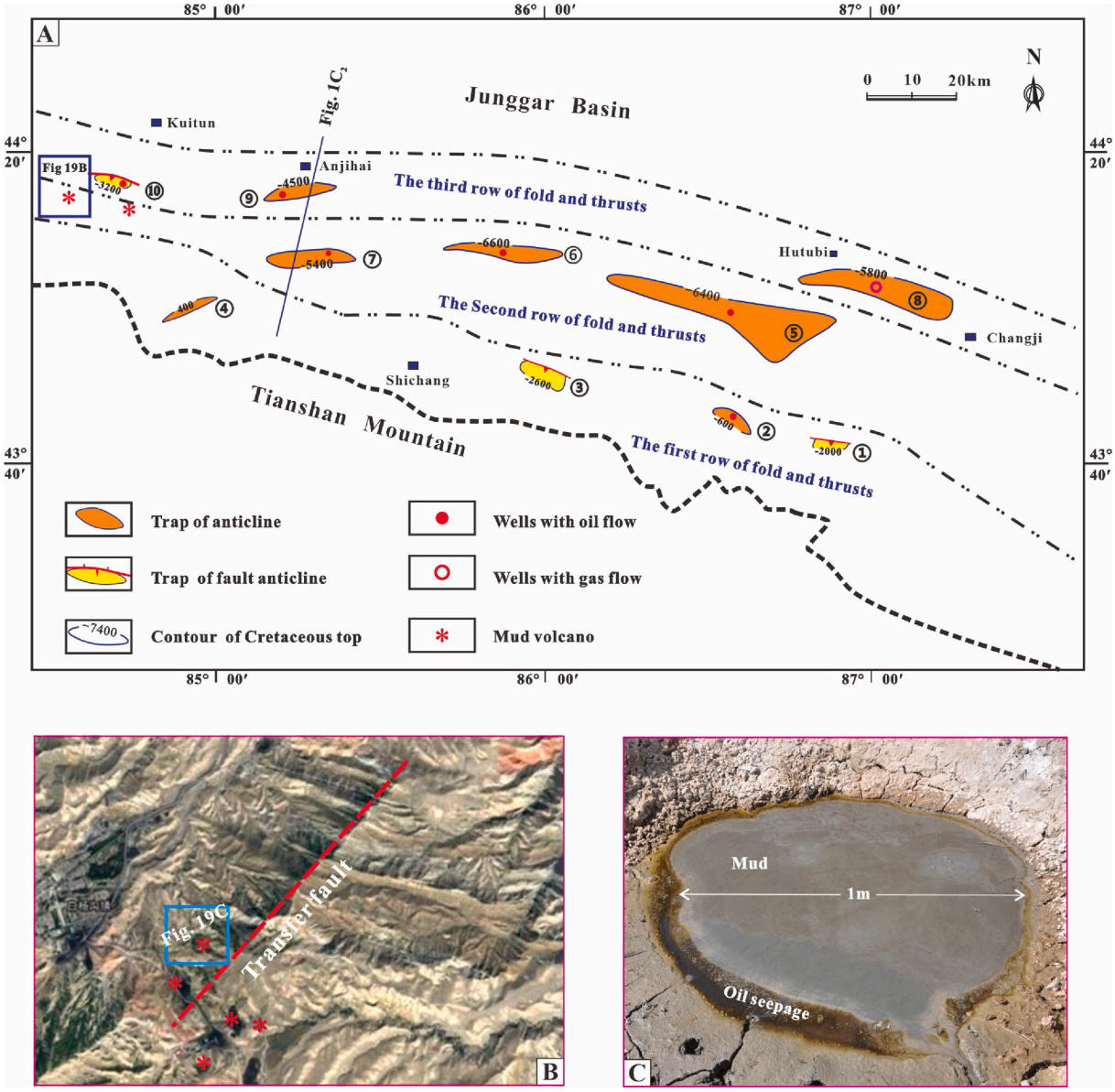

Fig. 19. a) Traps controlled by fold and thrust distribute in the western segment; b) remote sensing image to show the transfer fault location and c) the mud volcano and oil seepage.①-Changji fault anticline, ②-Qigu anticline,③-Qingshuihe anticline,④-Malasitai anticline,⑤-Tugulu anticline,⑥-Manasi anticline,⑦-Huoerguosi anticline,⑧-Hutubi anticline,⑨-Anjihai anticline,⑩-Dushanzi anticline.

with segmented structure in the western segment of the fold-and-thrust belts in the southern of the Junggar Basin. In the geological map, the fold-and-thrust belts can be divided into four segments (Fig. 2B), comparing to the four velocity modules in two numerical simulations. There are three rows of en echelon anticlines in the study area, and the strike of the deformation belts is northwest. Each fold-and-thrust belt comprises one anticline, and broad syncline develop between the rows of anticlines. The first row of fold and thrust which is piedmont thrust belt is controlled by large thrusts. Three rows of the fold and trusts in our simulation arrange oblique from the fast velocity module to lower one. The ductile layer isn't set at the backstop area, so the second row of fold and thrust appear next to the piedmont thrust belt without a syncline belt as a transition (Fig. 17). Another similarity between the simulation results and the nature case is the development of transfer faults. From the top view of the simulation, the Riedel shears under sinistral strike-slip movement are obvious (Fig. 17b). Four sub-segment regions are divided by sinistral strike-slip faults in the study area (Fig. 1B). Back-thrusts affected by dragging from the slower adjacent module in the both simulations are similar to the seismic interpretation in the southern margin of the Junggar Basin ((Figs. 18 and 1c).

The first row of fold-and-thrust belt of study area is characteristic as thick-skinned structures generated by basement-involved imbricate thrusts. This thick-skinned structure usually develops in the regions without the detachment layers such as mudstone and coal beds in the sediments. The homogenous simulation setting is similar to the rock sequence in the piedmont thrust belt, therefore, the simulation results show the basement-involved structures. Thin-skinned structures often develop under compression with detachment layers at the bottom. The deformation beds move above the Jurassic detachment layers to produce fault propagation folds in the hangingwall in the second and third row of fold and trusts in the southern of the Junggar Basin (Fig. 18b). The ductile layers at the wedge front absorbs the shortening bulk to cause a tight pop-up structure above the ramp-flat thrust that forms the thin-skinned structures. The ductile detachment simulation reproduced the process of this structure patterns in the front of the fold belts (Fig. 18a).

Our simulation results and previous analog models (Yu et al., 2009,

2012) in which there are two decollements and the shortening rate is 33%, they are fit well with the structural pattern developing in the western segment of the southern margin of the Junggar Basin. The results of the ductile detachment simulation suggest that two factors control the evolution in the western segment of the southern margin of the Junggar Basin: (i) the existence of the ductile detachment and (ii) the differential compression mechanism. There are several decollement beds with different thickness in the southern margin of Junggar Basin. We only set one thick weak layer similar to the total thickness of mudstone and coal beds from the Badaowan to the Xishanyao formations in the Jurassic system (Fig. 2) in the ductile detachment model to discuss its control action in order to increase the universality of the structural problems. In the future, these simulations would also extend to other study areas.

5.4. Insights into the oil and gas exploration

The southern margin of the Junggar Basin is very promising oil and gas exploration region with great potential (Sun et al., 2004; Guo et al., 2011; Chen et al., 2019). This simulation results are very useful to explain the factors that control the oil and gas distribution in the western segment of the northern margin in the Junggar Basin. There are mainly two patterns of traps bearing oil and gas that distribute along the fold and thrust belts in the western segment (Fig. 19a). The traps of fault anticline developed in the first row of the fold and thrust belts were controlled by the basement-involved structures. This kind of traps was first formed in the early shortening stage and became the higher topography in the piedmont thrust belt with the more compression amount (Fig. 19a). When the traps involved in the higher elevation level thrust to the surface, the reservoir will be eroded and cannot keep holding the oil and gas. Except the well drilled in the Qigu anticline trap with the oil flow, other wells did not succeed in the exploration. Therefore, we think that the first row of structural belts in the piedmont of the northern margins of the Tianshan Mountains are not prospecting areas. Other traps of anticlines developed in the second and the third row of the fold and thrust belts in the western segment were determined by the detachment fold structures above the viscous layers in Jurassic strata. This kind of traps developed in the Cretaceous sandstone layers and was sealed by Eocene mudstone. The oil and gas can migrate from the Jurassic source to the traps along the forward and backward thrust faults and accumulate into commercial oil field. Several wells drilled through this kind of traps in the Hutubi, Tugulu, Huoerguosi and Dushanzi anticlines all met oil flows (Fig. 1c). Therefore, the second and third rows of structural belts in the western segment should be regard as more favorable exploration regions. The transfer zones also play important role to the migration of the liquid fluid among pore with high pressure. When the transfer fault cut through the sealed rocks, the liquid fluid will migrate to the surface to form seepage and mud volcanoes, for example, the Dushanzi and Baiyanggou mud volcanoes in the western sub-segment of the southern margins of the Junggar Basin (Fig. 19b and c). In these kind regions, the lower traps in the Jurassic reservoirs sealed by the Lower Cretaceous are favorable for forming large-scale oil-gas field and should be paid more attention to exploration in the future (Guo et al., 2011).

6. Conclusion

Two differential compression simulations were conducted in this work to investigate the structural styles and kinematic evolution of the differential shortening fold-and-thrust belts, which raises the following major points:

(1) Resistance from the slower adjacent module can lead to back-thrusts prevailing in the faster module. Conversely, weak nucleation in the slower module is influenced by drag from the other side. The development of the piedmont thrust belt, gentle syncline, and pop-up structure are characteristic of the simulated ductile detachment.
(2) Two strike-slip fault systems are recognized in the differential compression simulation, Riedel shears at the foot of the backstop have a “flower structure,” which is composed of steep faults in the cross section, and the transfer faults in front appear flat thrusts with back-thrusts on the hangingwall.
(3) The results of these simulations identify two factors that control the structural patterns of the south margin of the Junggar Basin. Oblique and curved fold-and-thrust belts are generated from the differential compression, and multiple rows of anticline, such as the Huoerguosi and the Anjihai anticlines, are related to the ductile detachment.

Declaration of competing interest

The authors declare that they have no known competing financial interests or personal relationships that could have appeared to influence the work reported in this paper.

Data availability

No data was used for the research described in the article.

Acknowledgments

This study was funded by the National Natural Science Foundation of China, China (Grant No. 42072144) and Shengli Oilfield, SINOPEC, China (Grant No. 30200018-21-ZC0613-0030 and 30200018-20-ZC0613-0116). We thank Soumyajit Mukherjee and other two anonymous reviewers to improve both the content and presentation of this article with constructive and detailed comments. Suggestions and the detailed check of the expression from the Journal Editor, Alexander L Peace are also acknowledged.

References

Abe, S., van Gent, H., Urai, J.L., 2011. DEM simulation of normal faults in cohesive materials. Tectonophysics 512 (1–4), 12–21.
Adam, J., Urai, J.L., Wieneke, B., Oncken, O., Pfeiffer, K., Kukowski, N., Lohrmann, J., Hoth, S., van der Zee, W., Schmatz, J., 2005. Shear localisation and strain distribution during tectonic faulting—new insights from granular-flow experiments and high-resolution optical image correlation techniques. J. Struct. Geol. 27 (2), 283–301.
Ai, J., Chen, J.-F., Rotter, J.M., Ooi, J.Y., 2011. Assessment of rolling resistance models in discrete element simulations. Powder Technol. 206 (3), 269–282.
Aridhi, S., Aridhi, K., Ghanmi, M., Zargouni, F., Mercier, E., 2014. Structural context of meso-scale and cartographical duplex structure genesis in thrusting tectonics: role of tear faults. Zaghouan thrust belt. Case of Bir M'Cherga-Ain Asker area. Arabian J. Geosci. 7 (6), 2499–2514.
Bonnet, C., Malavieille, J., Mosar, J., 2007. Interactions between tectonics, erosion, and sedimentation during the recent evolution of the Alpine orogen: analogue modeling insights. Tectonics 26 (6), 1–15.
Borderie, S., Graveleau, F., Witt, C., Vendeville, B.C., 2018. Impact of an interbedded viscous décollement on the structural and kinematic coupling in fold-and-thrust belts: insights from analogue modeling. Tectonophysics 722, 118–137, 2018.
Bose, N., Mukherjee, S., 2020. Estimation of deformation temperatures, flow stresses and strain rates from an intra-continental shear zone: the Main Boundary Thrust, NW Himalaya (Uttarakhand, India). Mar. Petrol. Geol. 112 (2020), 1–15.
Calassou, S., Larroque, C., Malavieille, J., 1993. Transfer zones of deformation in thrust wedges: an experimental study. Tectonophysics 221 (3), 325–344.
Chemenda, A.I., Cavalié, O., Vergnolle, M., Bouissou, S., Delouis, B., 2016. Numerical model of formation of a 3-D strike-slip fault system. Compt. Rendus Geosci. 348 (1), 61–69.
Chen, J., Wang, X., Ni, Y., Xiang, B., Liao, F., Liao, J., Zhao, C., 2019. Genetic type and source of natural gas in the southern margin of Junggar Basin, NW China. Petrol. Explor. Dev. 46 (3), 482–495.
Cotton, J.T., Koyi, H.A., 2000. Modeling of thrust fronts above ductile and frictional detachments: application to structures in the Salt Range and Potwar Plateau, Pakistan. Geol. Soc. Am. Bull. 112 (3), 351–363.
Cundall, P.A., Strack, O.D.L., 1983. Modeling of Microscopic Mechanisms in Granular Material, Studies in Applied Mechanics. Elsevier, pp. 137–149.
Dean, S.L., Morgan, J.K., Fournier, T., 2013. Geometries of frontal fold and thrust belts: insights from discrete element simulations. J. Struct. Geol. 53, 43–53 (2013.

Deng, Q.-D., Feng, X.-Y., Zhang, P.-Z., Yang, X.P., Xu, X.W., Peng, S.Z., Li, J., 1999. Reverse fault and fold zone in the Urumqi range-front depression of the northern Tianshan and its genetic mechanism [in Chinese with English abstract]. Earth Sci. Front. 6 (4), 191–201.
Dooley, T., McClay, K., Bonora, M., 1999. Geological Society, London, petroleum Geology Conference series. In: 4D Evolution of Segmented Strike-Slip Fault Systems: Applications to NW Europe. Geological Society of London, pp. 215–225.
Fu, B., Lin, A., Kano, K.-i., Maruyama, T., Guo, J., 2003. Quaternary folding of the eastern Tian Shan, northwest China. Tectonophysics 369 (1–2), 79–101.
Furuichi, M., Nishiura, D., Kuwano, O., Bauville, A., Hori, T., Sakaguchi, H., 2018. Arcuate stress state in accretionary prisms from real-scale numerical sandbox experiments. Sci. Rep. 8 (1), 8685.
Graveleau, F., Malavieille, J., Dominguez, S., 2012. Experimental modelling of orogenic wedges: a review. Tectonophysics 538–540, 1–66, 2012.
Gray, G.G., Morgan, J.K., Sanz, P.F., 2014. Overview of continuum and particle dynamics methods for mechanical modeling of contractional geologic structures. J. Struct. Geol. 59, 19–36.
Groshong Jr., R.H., 1994. Area balance, depth to detachment, and strain in extension. Tectonics 13 (6), 1488–1497.
Guo, Z., Wu, C., Zhang, Z., Chen, W., 2011. Tectonic control on the hydrocarbon accumulation and prospect for large oil-gas field exploration in the southern Junggar basin [in Chinese with English abstract]. Geol. J. China Univ. 17 (2), 185–195.
Hardy, S., McClay, K., Muñoz, J.A., 2009. Deformation and fault activity in space and time in high-resolution numerical models of doubly vergent thrust wedges. Mar. Petrol. Geol. 26 (2), 232–248.
Hazzard, J.F., Mair, K., 2003. The importance of the third dimension in granular shear. Geophys. Res. Lett. 30 (13), 1708.
Iwashita, K., Oda, M., 1998. Rolling resistance at contacts in simulation of shear band development by DEM. J. Eng. Mech.
Jiang, M., Shen, Z., Wang, J., 2015. A novel three-dimensional contact model for granulates incorporating rolling and twisting resistances. Comput. Geotech. 65, 147–163, 2015.
Kh, A.B., Mirghasemi, A.A., Mohammadi, S., 2011. Numerical simulation of particle breakage of angular particles using combined DEM and FEM. Powder Technol. 205 (1–3), 15–29.
Li, C., 2019. Quantitative analysis and simulation of structural deformation in the fold and thrust belt based on Discrete Element Method. In: School of Earth Sciencs and Engineering. NANJING UNIVERSITY, Nanjing, China [in Chinese with English abstract].
Ma, D., Koyi, H.A., Yuan, J., He, D., Zhang, H., Wang, H., Wang, Y., Cui, J., 2019. The role of deep-seated half-grabens in the evolution of Huoerguosi-Manasi-Tugulu fold-and-thrust belt, northern Tian Shan, China. J. Geodyn. 131, 1–13, 2019.
Macedo, J., Marshak, S., 1999. Controls on the geometry of fold-thrust belt salients. Geol. Soc. Am. Bull. 111 (12), 1808–1822.
Martínez-Martínez, J.M., Booth-Rea, G., Azañón, J.M., Torcal, F., 2006. Active transfer fault zone linking a segmented extensional system (Betics, southern Spain): insight into heterogeneous extension driven by edge delamination. Tectonophysics 422 (1–4), 159–173.
McClay, K.R., 1990. Deformation mechanics in analogue models of extensional fault systems. Geol. Soc. 54 (1), 445–453. London, Special Publications.
Naylor, M.A., Mandl, G.t., Supesteijn, C.H.K., 1986. Fault geometries in basement-induced wrench faulting under different initial stress states. J. Struct. Geol. 8 (7), 737–752.
Potyondy, D.O., Cundall, P.A., 2004. A bonded-particle model for rock. Int. J. Rock Mech. Min. Sci. 41 (8), 1329–1364.
Razavi Pash, R., Davoodi, Z., Mukherjee, S., Dehsarvi, L.H., Ghasemi-Rozveh, T., 2021. Interpretation of aeromagnetic data to detect the deep-seated basement faults in fold thrust belts: NW part of the petroliferous Fars province, Zagros belt, Iran. Mar. Petrol. Geol. 133 (2021), 1–12.
Reber, J.E., Vidal, C.S., McLafferty, S., Mukherjee, S., 2021. Relationship between channel flow initiation and crustal viscosity in convergent settings: an analog modeling approach. Int. J. Earth Sci. 110 (6), 2057–2064.
Reiter, K., Kukowski, N., Ratschbacher, L., 2011. The interaction of two indenters in analogue experiments and implications for curved fold-and-thrust belts. Earth Planet Sci. Lett. 302 (1–2), 132–146.
Ruh, J.B., Gerya, T., Burg, J.-P., 2014. 3D effects of strain vs. velocity weakening on deformation patterns in accretionary wedges. Tectonophysics 615–616, 122–141, 2014.
Ruh, J.B., Gerya, T., Burg, J.P., 2013. High-resolution 3D numerical modeling of thrust wedges: influence of décollement strength on transfer zones. G-cubed 14 (4), 1131–1155.
Saltzer, S.D., Pollard, D.D.J.T., 1992. Distinct element modeling of structures formed in sedimentary overburden by extensional reactivation of basement normal faults. Tectonics 11 (1), 165–174.
Sun, C., Jia, D., Yin, H., Chen, Z., Li, Z., Shen, L., Wei, D., Li, Y., Yan, B., Wang, M., 2016. Sandbox modeling of evolving thrust wedges with different preexisting topographic relief: implications for the Longmen Shan thrust belt, eastern Tibet. J. Geophys. Res. Solid Earth 121 (6), 4591–4614.
Sun, Z.M., He, Z.L., Mou, Z.H., 2004. Structural features and favorable exploration areas in southern margin of Junggar basin [in Chinese with English abstract]. Oil Gas Geol. 25 (2), 216–221.
Taniyama, H., 2011. Numerical analysis of overburden soil subjected to strike-slip fault: Distinct element analysis of Nojima fault. Eng. Geol. 123 (3), 194–203.
van Gent, H.W., Holland, M., Urai, J.L., Loosveld, R., 2010. Evolution of fault zones in carbonates with mechanical stratigraphy – insights from scale models using layered cohesive powder. J. Struct. Geol. 32 (9), 1375–1391.
Wang, Y., Yu, F., Liu, Z., Wang, Y., Wang, Y., 2019. Two-dimensional discrete element simulation of plate subduction deformation process: an insight into the genesis of East China Sea Shelf Basin [in Chinese with English abstract]. Mar. Geol. Quat. Geol. 39 (5), 163–173.
Wenk, L., Huhn, K., 2013. The influence of an embedded viscoelastic–plastic layer on kinematics and mass transport pattern within accretionary wedges. Tectonophysics 608 (2013), 653–666.
Willett, S.D., 1992. Dynamic and Kinematic Growth and Change of a Coulomb Wedge, Thrust Tectonics. Springer, pp. 19–31.
Wu, Z., Yin, H., Wang, X., Zhao, B., Jia, D., 2014. Characteristics and deformation mechanism of salt-related structures in the western Kuqa depression, Tarim basin: insights from scaled sandbox modeling. Tectonophysics 612–613, 81–96, 2014.
Yu, F., Li, G., Yang, G., Ma, B., Chen, S., 2009. Deformation feature and genesis simulation of fold-and-Thrust belts in the southern margin, Junggar Basin [in Chinese with English abstract]. Geotectonica Et Metallogenia 33 (3), 386–395 [in Chinese].
Yu, F., Li, X., Li, D., Feng, Z., Li, X., 2012. Simulation for the controlling factors of structural deformation in the southern margin of the Junggar Basin. Acta Geol. Sin.-English Ed. 86 (4), 842–853.
Zhang, J., Morgan, J.K., Gray, G.G., Harkins, N.W., Sanz, P.F., Chikichev, I., 2013. Comparative FEM and DEM modeling of basement-involved thrust structures, with application to Sheep Mountain, Greybull area, Wyoming. Tectonophysics 608, 408–417.
Zhou, B., Huang, R., Wang, H., Wang, J., 2013. DEM investigation of particle anti-rotation effects on the micromechanical response of granular materials. Granul. Matter 15 (3), 315–326.
Zhou, Y., Yu, F., Liu, Z., 2019. Superimposed extensional deformation of different layers: insights from two dimensional discrete element modeling [in Chinese with English abstract]. Geotect. Metallogenia 43, 213–225, 02.
Zweigel, Peter, 1998. Arcuate accretionary wedge formation at convex plate margin corners: results of sandbox analogue experiments. Journal of Structural Geology 20 (12), 1597–1609.